Thermal Damage Control for Dry Grinding of MgO/CeO2 Glass Ceramic

Qu, M., Jin, T., Xie, G., Cai, R. & Lu, A.

Original citation & hyperlink:
Qu, M, Jin, T, Xie, G, Cai, R & Lu, A 2019, 'Thermal Damage Control for Dry Grinding of MgO/CeO2 Glass Ceramic', The International Journal of Advanced Manufacturing Technology, vol. 105, pp. 3387-3396.
https://dx.doi.org/10.1007/s00170-019-04460-0

DOI 10.1007/s00170-019-04460-0
ISSN 0268-3768
ESSN 1433-3015

Publisher: Springer

The final publication is available at Springer via http://dx.doi.org/10.1007/s00170-019-04460-0

Thermal Damage Control for Dry Grinding of MgO/CeO_2 Glass Ceramic

Meina Qu[a, b], Tan Jin[a, b], Guizhi Xie[a,b,*], Rui Cai[c], Jun Yi[a, b,d], Ange Lu[a, b]

[a] National Engineering Research Centre for High Efficiency Grinding, Hunan University, Changsha, Hunan 410082, China

[b] College of Mechanical and Vehicle Engineering, Hunan University, Changsha, Hunan 410082, China

[c] School of Mechanical, Aerospace and Automotive Engineering Faculty of Engineering Environment and Computing, Coventry University, 3 Gulson Road, Coventry, CV1 2JH, UK

[d] Intelligent Manufacturing Institute of HNUST, Hunan University of Science and Technology, Xiangtan 411201, China

* Corresponding author. Tel.: +86 731 88821833; fax: +86 731 88823921. E–mail address: guizhixie@hnu.edu.cn

Thermal Damage Control for Dry Grinding of MgO/CeO_2 Glass Ceramic

Abstract: MgO/CeO_2 glass ceramic is a key solid catalyst and accelerant produced by raw mixing, prilling and pressure sintering. Grinding, as a high–efficiency machining method was used to obtain MgO/CeO_2 glass ceramic components with accurate size to meet the size requirements of design. However, thermal damage occurring on the ground surface may change the properties of the components and affect their performance in subsequent applications. In this work, a grinding thermal model was established and validated by experiments. On the basis of this thermal model, the grinding temperature can be controlled to < 100 °C by selecting optimal grinding parameters and thus prevent grinding burn. The mechanism of potential chemical reactions on the grinding surface was further studied by analysing the transient temperature jump at a grain wear flat area and comparing the change in element mass fraction before and after grinding. The performance of a normal resin–bond diamond wheel and a resin–bond wheel with Ni–P alloy coating on the diamond grains was compared. Results showed that the latter intensified the redox reaction because of the catalytic actions of Ni and P, and the mass fraction of each elements on the workpiece surface shows obvious uneven distribution due to the surface spalling of Ni–P alloy. All these results indicated that key issues are the optimal setup of process parameters to control the grinding–zone temperature and the selection of a proper grinding wheel to avoid catalytic elements such as Ni and P.

Keywords: MgO/CeO_2 glass ceramic; thermal damage; grinding thermal model; transient temperature; chemical reactions

Nomenclature

B_s	workpiece width
l_c	length of wheel/work contact arc

v_w	worktable speed
v_s	wheel speed
R_s	radii of the outer rings of grinding wheel
R_o	radii of the inner rings of grinding wheel
d_s	grinding wheel diameter
Q	heat flux density
Q_d	heat flux density of point heat source
Q_l	heat flux density of line heat source
Q_s	heat flux density of surface heat source
$\bar{Q}_s$	average heat flux density of surface heat source
T_l	temperature caused by a linear heat source
T_s	temperature caused by surface heat source
T_{sd}	transient temperature at grain wear flat
c	specific heat capacity of the workpiece
ρ	density
a_p	grinding wheel depth of cut
α	thermal diffusivity of workpiece
α_g	thermal diffusivity of abrasive grain
t_a	undeformed grinding chip thickness
Q_t	total grinding heat flux
Q_w	heat flux partitioned to the workpiece

q_s	heat flux partitioned to the grinding wheel
Q_{sg}	heat flux partitioned to single abrasive grain
R_{wch}	energy partition between the workpiece and grinding chips
R_{ws}	energy partition to the workpiece in workpiece–wheel subsystem
R_w	energy partition to the workpiece
N_d	dynamic cutting edge density
N_s	static cutting edge density
k_g	thermal conductivity of the abrasive grits
β_w	thermal property of the workpiece
r_o	effective radius of the abrasive grain contact
t	grinding time

1. Introduction

MgO/CeO_2 glass ceramic, as a solid basic catalyst, can be used in the transesterification of triglycerides to biodiesel [1, 2] and degradation of phenol wastewater through catalytic ozonation [3]. MgO/CeO_2 glass ceramic is also a key accelerant for producing of high–strength and high–density silicon nitride [4] and silicon carbide [5]. After raw mixing, prilling, and pressure sintering, the dimension accuracy of MgO/CeO_2 glass ceramic could not meet the size requirements of design; thus, the ceramic cannot easily enter the combustion chamber through transport channel. Grinding with resin bond diamond cup wheel is an effective method to process to meet the size accuracy and surface quality for such hard and brittle materials [6]. However, the heat transferred into the workpiece increases its temperature, leading to grinding burn. The transient high–temperature at grain wear flat may cause chemical reactions,

which change the physical properties and affect the performance of MgO/CeO_2 glass ceramic in subsequent applications.

The increase in grinding temperature can be predicted by thermal models and measured by thermocouples. Thermal models, such as gears in form grinding [7], cylindrical grinding [8], high–efficiency deep grinding [9] have been developed for analysing heat transfer problems in grinding during the past decades. In recent years, some scholars have studied thermal models for grinding, such as cup grinding wheels [10, 11], intermittent grinding wheels [12], and engineered grinding wheel [13], by grinding wheels of specific shapes. Wang et al. proposed that for thermal models of cup grinding wheels, an analytical thermal model of annular moving heat source for large surface workpiece should be used [10]. Zhang et al. developed an analytical thermal model of arc moving heat source for rectangular workpiece [11]. However, these thermal models are complex and not suitable for grinding narrow–strip workpiece by a cup wheel. For testing grinding temperature, Xu et al. compared three temperature measuring techniques (embedded thermocouple, two colour infrared detectors, and foil/workpiece thermocouple) to estimate the energy partition in grinding [14]. Xie et al. measured the grinding temperature of yttria that was partially stabilized by zirconia in HEDG by using the thermocouple technique [15]. Chen et al. measured the grinding temperature by using a fibre bragg grating and verified the corresponding results [16]. Establishing the thermal model with verification via experiments can guide the selection of grinding parameters, effectively control the heat input into the grinding zone and prevent grinding burn. However, the transient temperature at grain wear flat is considerably higher than the grinding temperature rise [17]. However, the high temperatures at the grain wear flat that can induce the grinding burn, chemical reactions may occur in the contact zone because of the complex composition of the grinding wheels [18] in high transient temperatures.

This study established a grinding thermal model to prevent thermal damage during

the dry grinding of MgO/CeO_2 glass ceramic. Temperature experiments under different processing conditions were used to validate the thermal model. The mechanism of potential chemical reactions on the grinding surface was also studied by analysing the transient temperature jump at the grain wear flat area and comparing the change of element mass fraction before and after grinding.

2. Thermal model

2.1 Derivation of the thermal model

Fig. 1 shows a typical surface grinding mode by using a cup wheel. The grinding width is equal to the workpiece width (B_s). The grinding wheel moves along the workpiece surface in worktable speed (v_w); R_s and R_o are the radii of the outer and inner rings of the wheel, respectively. The contact area between the wheel and workpiece forms a circular band. This circular band heat source, with a finite length and width, moves along the workpiece surface, thereby increasing the temperature in the workpiece, on and beneath the surface.

B_s is considerably smaller than the diameter of the grinding wheel (d_s); thus, the circular band heat source can be simplified into a rectangle heat source of constant heat with length B_s and width $R_s - R_o$. The rectangular heat source moves with velocity, v, along the x direction. As point heat source superposition is a useful method to solve the grinding temperature, the rectangular heat source is composed of line heat source, which is composed of point heat source for the surface grinding mode using a cup wheel.

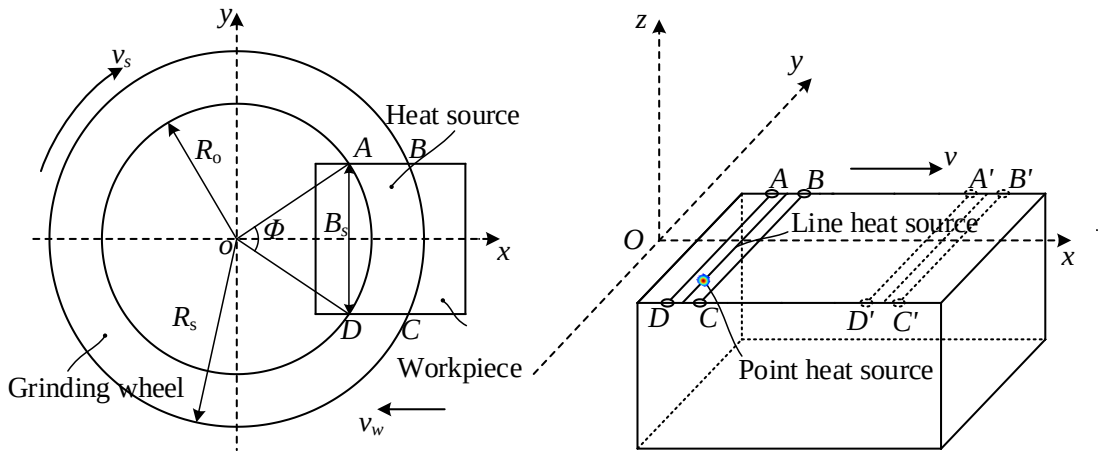

Fig. 1 Schematic of the cup wheel surface grinding process

In consideration of the line within the contact area, with radius R ($R_o \le R \le R_s$) and heat flux density Q_l, a unit element on the line can be regarded as a point heat source. The temperature increase caused by this unit elementis as follows [19]:

$$dT = \frac{Q_d dy_i}{c\rho\left(4\cdot\pi\cdot\alpha\cdot t\right)^{3/2}}\cdot e^{-\frac{\left(x-R\right)^2+\left(y-y_i\right)^2+z^2}{4\alpha\cdot t}} \tag{1}$$

Where Q_d is heat flux density of point heat source, c is the specific heat capacity of the workpiece, ρ is the density of workpiece, ans α is the thermal diffusivity of the workpiece.

The circular line can be regarded as a straight line, with x_i as its position in the x direction to simplify the analysis. The temperature increase caused by the line heat source with finite length, $l_c = y_2 - y_1$, can be expressed as follows:

$$T_l = \frac{Q_l}{c\rho\left(4\cdot\pi\cdot\alpha\cdot t\right)^{3/2}}\cdot e^{-\frac{(x-x_i)^2+z^2}{4\alpha\cdot t}}\cdot\int_{y_1}^{y_2} e^{-\frac{\left(y-y_i\right)^2}{4\alpha\cdot t}}\,dy_i \tag{2}$$

$$\int_{y_1}^{y_2} e^{-\frac{(y-y_0)^2}{4at}} dy_0 = \frac{\sqrt{4\pi at}}{2} \cdot [erf(\frac{y-y_1}{\sqrt{4\cdot\alpha\cdot t}}) - erf(\frac{y-y_2}{\sqrt{4\cdot\alpha\cdot t}})] \quad (3)$$

$$Ker(y) = \frac{1}{2} \cdot [erf(\frac{y-y_1}{\sqrt{4\cdot\alpha\cdot t}}) - erf(\frac{y-y_2}{\sqrt{4\cdot\alpha\cdot t}})] \quad (4)$$

Where: $y_1 = -\frac{B_s}{2}$, $y_2 = \frac{B_s}{2}$.

Accordingly, the temperature rise caused by the line heat source with finite length can be derived as follows:

$$T_l = Ker(y) \cdot \frac{Q_l}{c\rho(4\cdot\pi\cdot\alpha\cdot t)} \cdot e^{-\frac{(x-x_i)^2+z^2}{4\alpha\cdot t}} \quad (5)$$

The line heat source moves with velocity, v, along the x direction. Given the coordinate system in Fig. 1 as a moving system, the temperature rise caused by the moving line heat source at point (x, y, z) adjacent to the heat source for a time period t, the temperature fields of the workpiece can be expressed as follows:

$$T_l = Ker(y) \cdot \frac{Q_l}{c\rho(4\cdot\pi\cdot\alpha\cdot\tau)} \int_0^t \frac{d\tau}{\tau} \cdot e^{-\frac{(x-x_i)^2+z^2}{4\alpha\cdot\tau}} \cdot e^{-\frac{v^2\tau}{4\alpha}} \cdot e^{-\frac{(x-x_i)v}{4\alpha}} \quad (6)$$

Where $\omega = \frac{v^2\tau}{4\alpha}$; $u = \frac{v\cdot\sqrt{(x-x_i)^2+z^2}}{2\alpha}$.

$$T_l = Ker(y) \cdot \frac{Q_l}{c\rho(4\cdot\pi\cdot\alpha\cdot\tau)} \cdot e^{-\frac{(x-x_i)v}{4\alpha}} \cdot \int_0^{\frac{v^2 t}{4\alpha}} \frac{d\omega}{\omega} e^{-\omega-\frac{u^2}{4\omega}} \quad (7)$$

Once a steady state $\omega > 1.5$ is reached, the temperature fields of the workpiece can be expressed as follows:

$$T_l = Ker(y)\cdot\frac{Q_l}{c\rho\left(4\cdot\pi\cdot\alpha\cdot\tau\right)}\cdot e^{-\frac{(x-x_i)v}{4\alpha}}\cdot\int_0^{\infty}\frac{d\omega}{\omega}\cdot e^{-\omega-\frac{u^2}{4\omega}} \quad (8)$$

$$T_l = Ker(y)\cdot\frac{Q_l}{2\pi c\rho\alpha}\cdot K_0(u)\cdot e^{-\frac{(x-x_i)v}{2\alpha}} \quad (9)$$

Where $K_0(u)=\frac{1}{2}\int_0^{\infty}\frac{d\omega}{\omega}e^{-\omega-\frac{u^2}{4\omega}}$ is the zero–order Bessel function.

The grinding heat source is the summation of the moving line sources between the outer and inner rings of the wheel.

$$T_s = Ker(y)\cdot\frac{Q_s}{2\alpha\pi c\rho}\int_{R_o}^{R_s}K_0\left(\frac{v\sqrt{(x-x_i)^2+z^2}}{2\alpha}\right)\cdot e^{-\frac{(x-x_i)v}{2\alpha}}dx_i \quad (10)$$

Where Q_s is heat flux partitioned to the grinding wheel, and R_s and R_0 are the radii of the outer and inner rings of the wheel, respectively.

In consideration of the semi–infinite gross and the heat source as a triangular distribution, the temperature fields of the workpiece can be calculated using Formula 11 as follows:

$$T_s = 2Ker(y)\cdot\frac{\overline{Q_s}}{\alpha\pi c\rho}\int_{R_o}^{R_s}\frac{x_i\text{-}R_o}{R_s-R_o}K_0\left(\frac{v\sqrt{(x-x_i)^2+z^2}}{2\alpha}\right)\cdot e^{-\frac{(x-x_i)v_w}{2\alpha}}dx_i \quad (11)$$

As shown in Fig. 2, the transient temperature at the top of the wear flat area of a single grain is considerably higher than that on the overall workpiece surface that may cause chemical reactions at the local contact area. The shape of an average single grain particle was simplified as a small cone to calculate the temperature at the top of the wear flat area of a single grain. Assuming that only one–dimensional conduction occured in the direction vertical to the grinding surface, the contact time t can be expressed as $t = l_c/v_w$, and the transient temperature at grain wear flat T_{sd} can be

calculated in accordance with Formula 12 as follows:

$$T_{sd} = \frac{Q_{sg}}{k_g}\sqrt{\frac{4a_g t}{\pi}} \quad (12)$$

Where Q_{sg} is heat flux partitioned to single abrasive grain, k_g is thermal conductivity of the abrasive grits and α_g is thermal diffusivity of the abrasive grain.

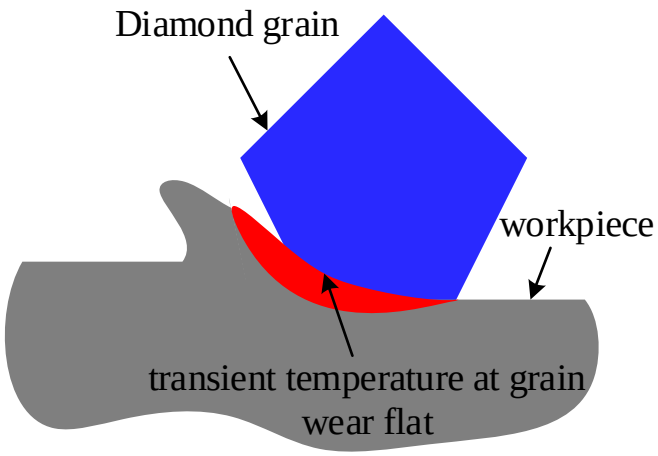

Fig. 2 Schematic of grinding temperature rise and transient temperature at grain wear flat

2.2 Grinding heat partition analysis

The total grinding heat generated at the wheel–work contact area under dry grinding conditions was transferred into the workpiece, grinding wheel and grinding chips through conduction. Jin and Stephenson analysed the variation in heat partition ratio to the grinding chips and convection heat transfer coefficient of grinding fluids under different grinding parameters. Comprehensive thermal modelling approaches combining heat transfer to different parts, including the workpiece, abrasive grits, grinding chips, and grinding fluids, were developed [20]. In accordance with this work, the heat partition ratio to the workpiece R_w under dry grinding condition can be calculated as follows:

$$R_w = \frac{R_{ws} \cdot R_{wch}}{R_{ws} + R_{wch} - R_{ws} \cdot R_{wch}} \quad (13)$$

$$R_{ws} = \left[1 + \frac{0.97 k_g}{\beta_w \cdot \sqrt{r_0} \cdot v_s}\right]^{-1} \quad (14)$$

$$R_{wch} = \frac{1}{1 + 0.753\sqrt{\frac{v_s \cdot t_a}{\alpha \cdot \gamma}}} \quad (15)$$

Where R_{ws} is the energy partition to the workpiece in the workpiece–wheel subsystem, R_{wch} is the energy partition between the workpiece and the grinding chips, k_g is the thermal conductivity of the abrasive grits, t_a is the undeformed grinding chip thickness, β_w is the thermal property of the workpiece and α is the thermal diffusivity of the workpiece.

The total heat flux density of the grinding area Q_t under different grinding parameters can be obtained by using Formula 16.

$$Q_t = \frac{F_t \cdot v_s}{(R_s - R_0) \cdot B_s} \quad (16)$$

The heat flux partitioned to workpiece Q_w can be calculated as follows:

$$Q_w = Q_t R_w \quad (17)$$

The heat flux partitioned to abrasive q_s can be calculated as follows:

$$q_s = \frac{Q_w}{R_{ws}}(1 - R_{ws}) \quad (18)$$

The heat flux partitioned to a single abrasive grain Q_{sg} can be calculated as follows:

$$Q_{sg} = Q_s / (N_d \cdot \pi \cdot r_0^2) \quad (19)$$

Where N_d is the dynamic cutting-edge density and r_o is the effective radius of the

abrasive grain contact. In a typical precision grinding process, the radius of the grain top flat area r_0 is approximately 5 – 20 μm [21, 22], depending on the abrasive grain size and wear status. A value of 15 μm for the grain top flat radius is used in the present work.

3. Experimental details

3.1 Workpiece

MgO/CeO_2 glass ceramic was used as workpiece material (width: 6 mm, length: 10 mm) in the grinding tests. Density was measured in accordance with Archimedes' principle. Vickers micro–hardness was measured using a model 401/402 MVATM micro–indentation instrument made by Wilson after cutting and inlaying. Table 1 lists the physical and mechanical properties.

Table 1 Physical and mechanical properties of MgO/CeO_2 glass ceramic

Density, ρ (kg/m^3)	6,500
Hardness, H_v (Gpa)	14
Thermal conductivity, k (W/mK)	9.4
Specific heat, c (J/kgK)	850
Thermal expansion coefficient, ($\alpha\times10^{-6}$)	1.7014

3.2 Grinding experimental platform

Grinding experiments were carried out on a MK2945C grinding machine with six CNC axes (X, Y, Z, U, A and C). The X and Y axes movement has a control resolution of 0.1 μm. The positioning accuracy on the down reversing point of the Z–axis is within 0.05 mm. Grinding forces were monitored during the tests by a Kistler 9257B dynamometer. The grinding temperature was measured using a K–Thermocouple. The surface characteristics and element distribution were observed and detected through

scanning electron microscopy (SEM) and energy disperse spectroscopy (EDS). Fig. 3 shows the grinding test platform.

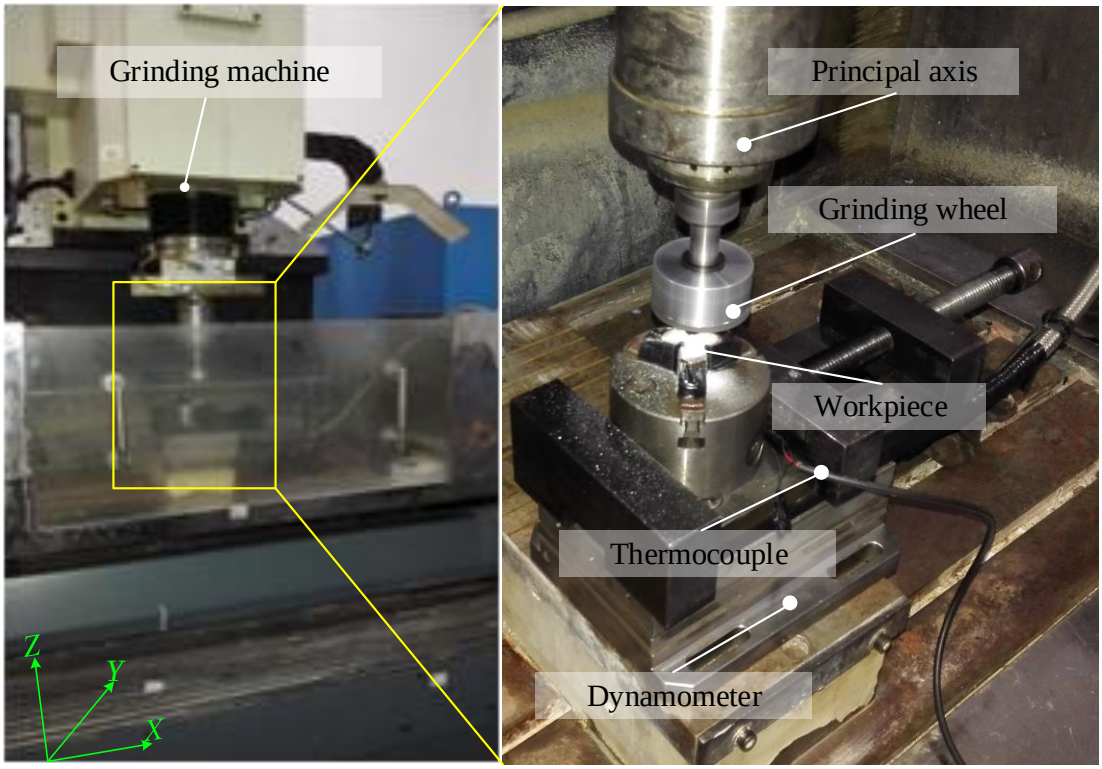

Fig. 3 Grinding test platform

Table 2 Grinding parameters

Grinding wheel	I: Resin bond Diamond wheel II: Resin bond Diamond wheel
Diameter of the wheel	50mm (abrasive zone： $R_s - R_o = 7$ mm)
Wheel speed v_s	15.7 m/s (maximum at the wheel front edge)
Worktable speed v_w	15 – 30 mm/s
Depth of cut a_p	10 – 50 μm
Grinding width B_s	7 mm

Grinding fluid	None

3.3 Grinding wheels

In this work, two types of resin–bonded diamond grinding wheel were used. The concentration of the grinding wheels was 100 %, average grit size was approximately 151 μm, and hardness of K was similar but with different additives. Fig. 4a shows an ordinary resin–bonded diamond grinding wheel. In Fig. 4b, a layer of Ni–P alloy is covered on the diamond abrasive particles to increase the infiltration and enhance the bonding strength of resin–bonded to the diamond abrasive particles and to extend its service life.

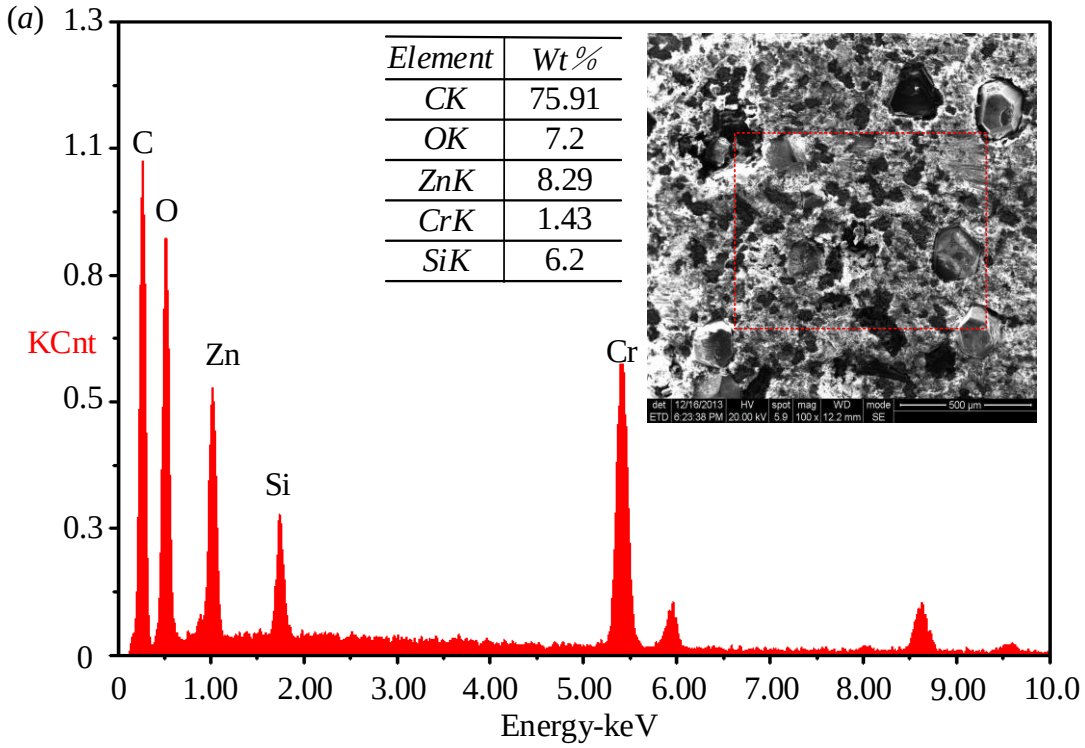

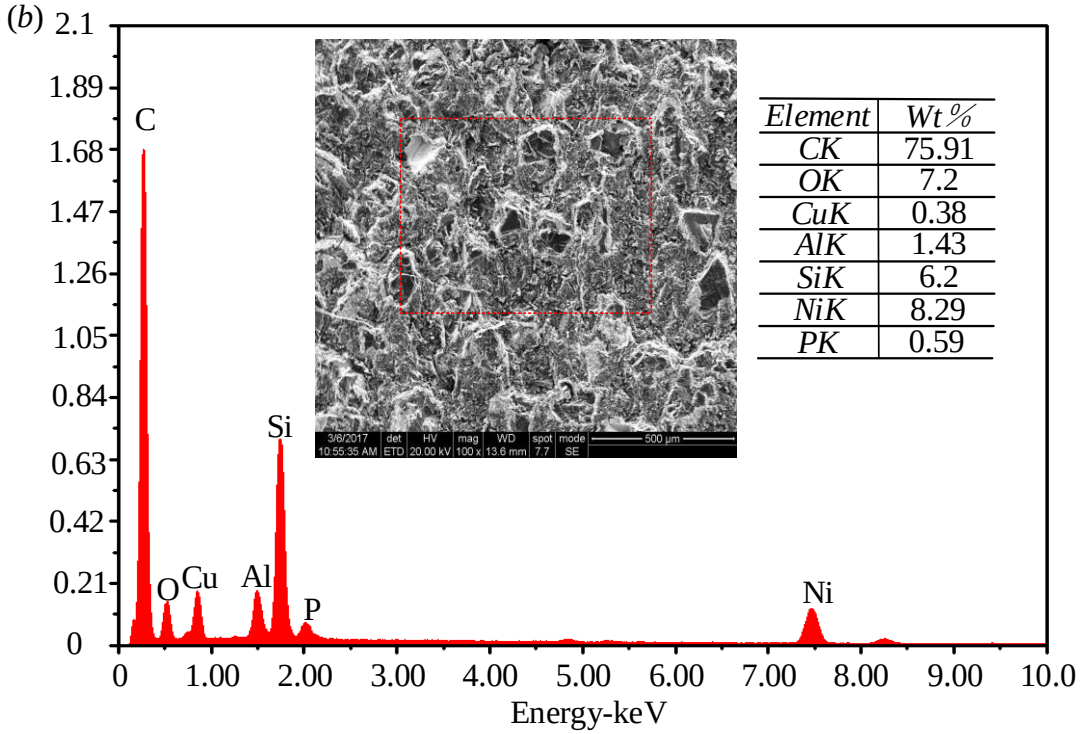

Fig. 4 Element distribution by EDS of grinding wheel (a) I and (b) II

4. Results

4.1 Grinding temperatures

Table 3 shows the experimental process parameters, cutting force measurement results, heat resource intensity, and temperature rise. Under the same machining parameters, the increase in calculated grinding temperature based on the thermal model was slightly lower than the increase in experimental grinding temperature.

Table 3 Experimental process parameters, cutting force measurement results, heat resource intensity, analytical and experimental temperature rise on workpiece surface and transient temperature at grain wear flat

No.	a_p (μm)	v_s (m/s)	v_w (mm/s)	F_t (N)	R_w	Analytical Temperature rise (ºC)	Experimental Temperature rise (ºC)	Transient temperature at grain wear flat T_{sd} (ºC)

1	10	15.7	15	5.2	0.094	32.26	39	840.26
2	20	15.7	15	5.9	0.093	38.31	47	1095.72
3	30	15.7	15	6.8	0.093	44.36	51	1341.85
4	40	15.7	15	7.6	0.093	46.37	55	1487.93
5	30	15.7	20	7.8	0.093	50.40	65	1385.48
6	30	15.7	25	8.3	0.093	52.42	66	1360.68
7	30	15.7	30	10.2	0.092	62.50	77	1501.20

Fig. 5 shows the comparison results of the calculated temperature rise with the values obtained via the K–Thermocouple. With increasing grinding depth, the grinding temperature rise increased (Fig. 5a). Figs. 5b and 5c show the distribution of grinding temperature rise accordance with the thermal model and the acquisition of temperature signal at the machining parameters of v_s = 15.7 m/s, v_w = 15 mm/s and a_p = 30 μm.

With the increasing worktable speed of the machining tool, the grinding temperature gradually increased (Fig. 6a). Figs. 6b and 6c show the distribution of grinding temperature rise in accordance with the thermal model considered and the acquisition of temperature signal at the machining parameters of v_s = 15.7 m/s, v_w = 30 mm/s and a_p = 30 μm.

The calculated temperature rise was slightly lower than the experimental measurements, but both exhibited an increasing trend. The results showed that the proposed thermal model can be used to predict the temperature during cup wheel. The maximum experimental temperature rise was approximately 77 ºC under the machining parameters of v_s = 15.7 m/s, v_w = 30 mm/s, and a_p = 30 μm, and it can meet the requirement for machining efficiency and control of grinding temperature within 100 ºC at room temperature.

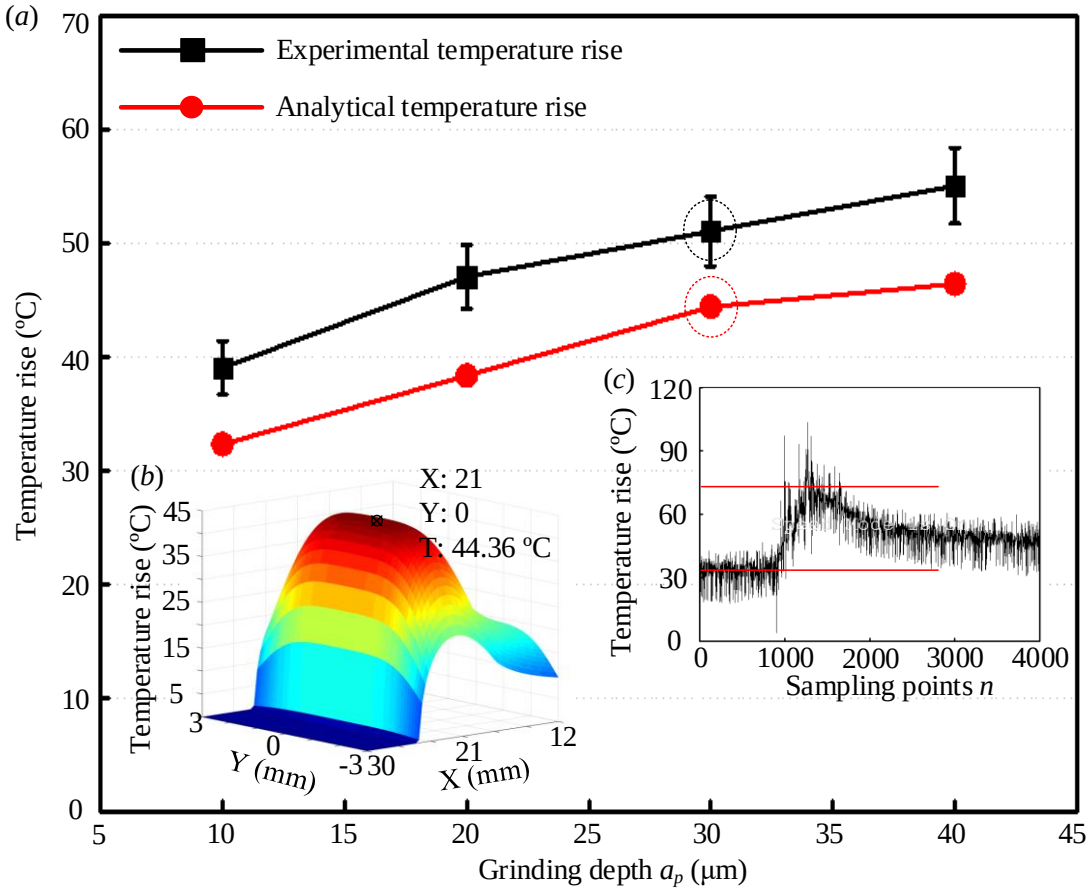

Fig. 5 Comparison of theoretical and experimental grinding temperature on the grinding surface (a) with grinding depth, (b) distribution of grinding temperature rise under v_s = 15.7 m/s, v_w = 15 mm/s and a_p = 30 μm, and (c) temperature signal acquisition under v_s = 15.7 m/s, v_w = 15 mm/s and a_p = 30 μm

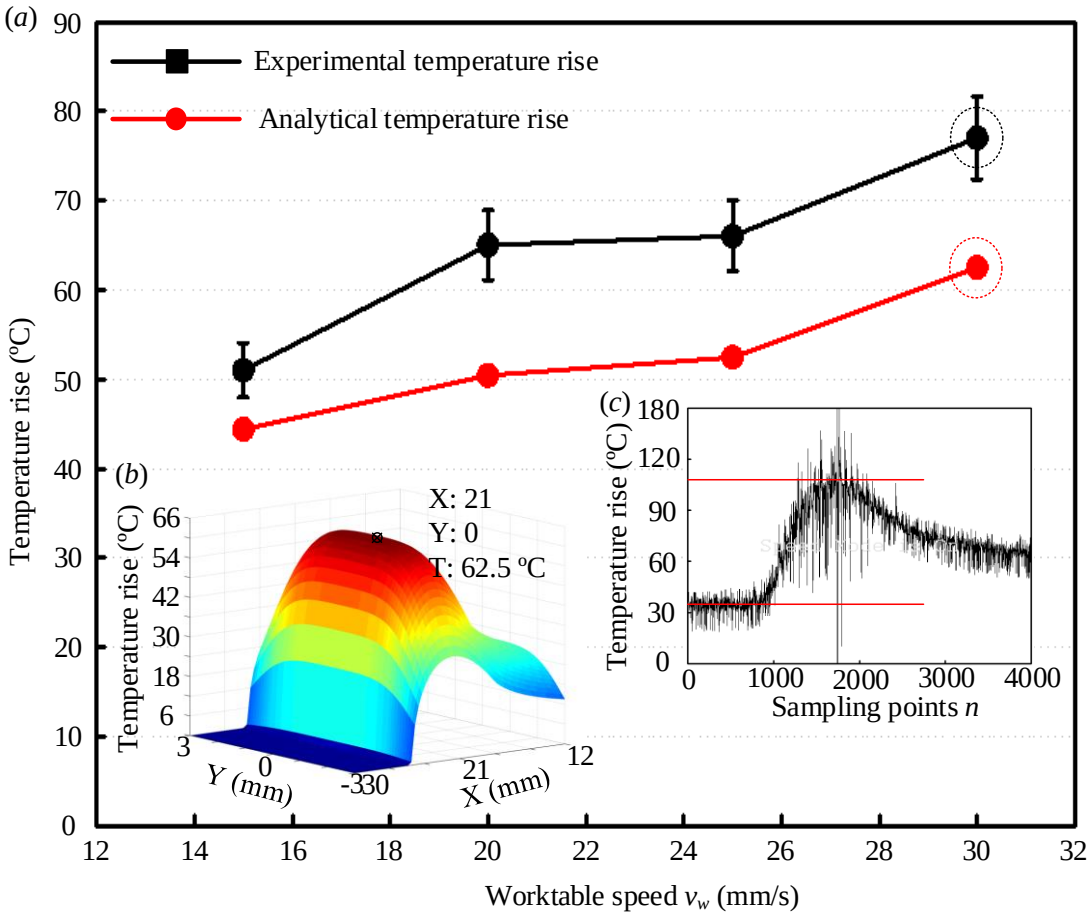

Fig. 6 Comparison of theoretical and experimental grinding temperature on the grinding surface: (a) with machining tool worktable speed, (b) distribution of grinding temperature rise under v_s = 15.7 m/s, v_w = 30 mm/s and a_p = 30 μm, and (c) temperature signal acquisition under v_s = 15.7 m/s, v_w = 30 mm/s and a_p = 30 μm

4.2 Surface characteristics of the ground surface

Fig. 7a shows the surface characteristics after sintering of MgO/CeO_2 glass ceramic, where the grains are evenly distributed, and the grain size distribution is concentrated. Figs. 7*b* and 7*c* show the surface characteristics after grinding by using grinding wheels I and II under v_s = 15.7 m/s, v_w = 30 mm/s and a_p = 30 μm. The experimental temperature by grinding wheels I and II almost did not have any difference, with less than 100 ºC under room temperature. No remarkable burn crack

was observed on the grinding surface in the secondary image. As shown in Fig. 7b, the light and heavy elements presented a homogeneous distribution in the backscattered electron image. However, as shown in Fig. 7c, the light and heavy elements were unevenly distributed in the backscattered electron image.

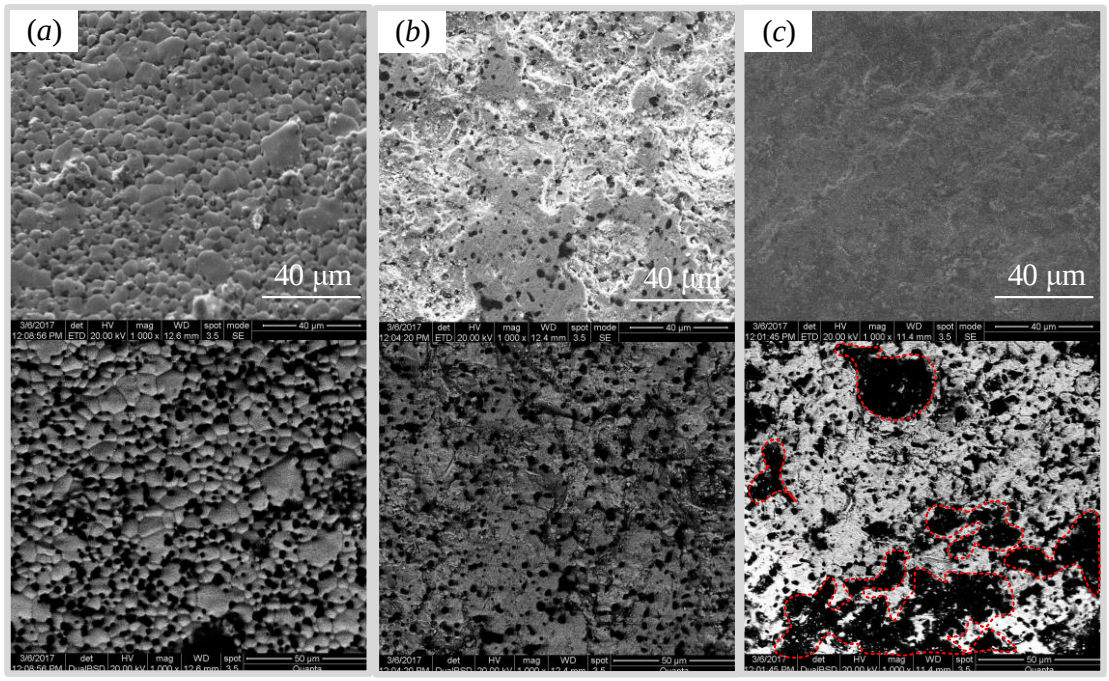

Fig. 7 Surface characteristics of (a) workpiece before grinding and after grinding by using grinding wheels (b) I (c) II

4.3 Chemical element distribution on the ground surface

EDS was used to study the change of chemical elements on the ground surface to further investigate the causes of the difference of light and heavy elements distribution (Fig. 8). Fig. 8a shows that the MgO/CeO_2 glass ceramic contain C, O, Mg, Ce and F before grinding. Fig. 8b shows the energy spectrum of the surface of the workpiece ground by wheel I and containing C, O, Mg, Ce and F. Fig. 8c shows the energy spectrum of a certain area on the surface of the workpiece ground by wheel II with added Ni and P.

(*a*)

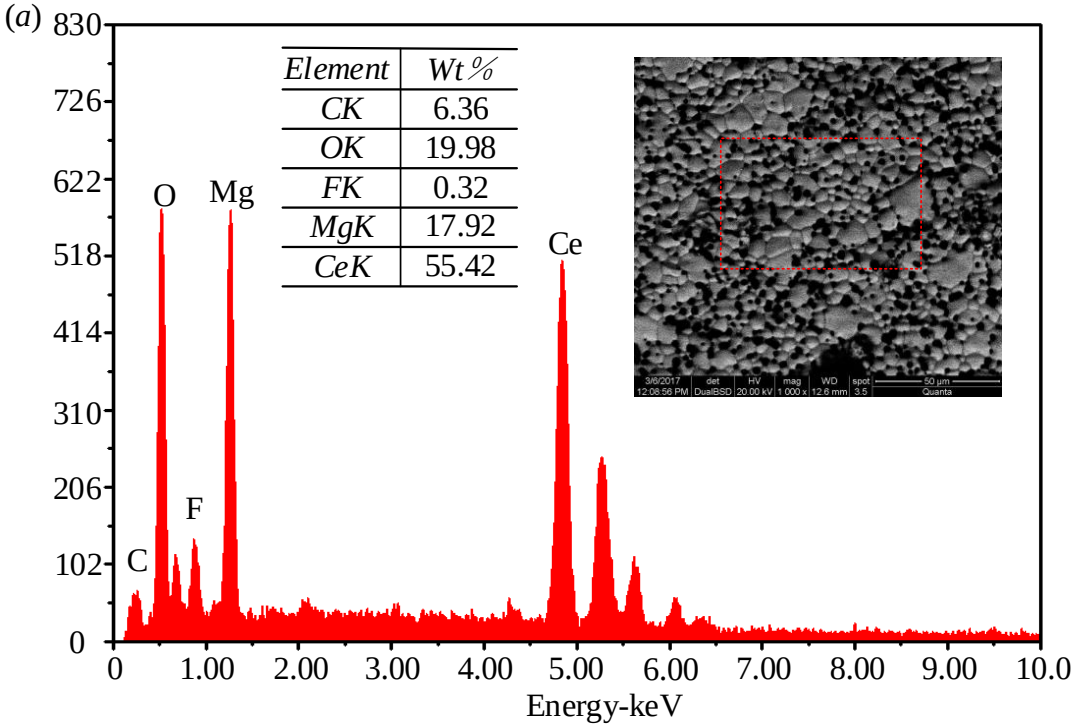
Element Wt%
CK 6.36
OK 19.98
FK 0.32
MgK 17.92
CeK 55.42
O
Mg
Ce
F
C
830
726
622
518
414
310
206
102
0
0 1.00 2.00 3.00 4.00 5.00 6.00 7.00 8.00 9.00 10.0
Energy-keV

(*b*)

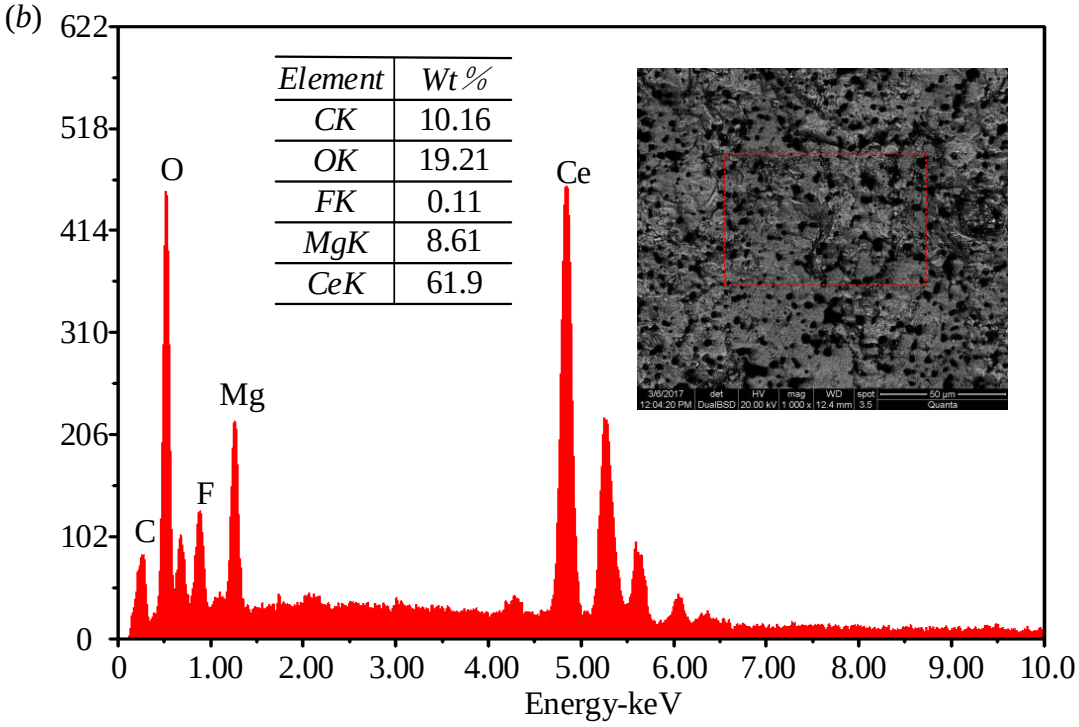
Element Wt%
CK 10.16
OK 19.21
FK 0.11
MgK 8.61
CeK 61.9
O
Ce
Mg
F
C
622
518
414
310
206
102
0
0 1.00 2.00 3.00 4.00 5.00 6.00 7.00 8.00 9.00 10.0
Energy-keV

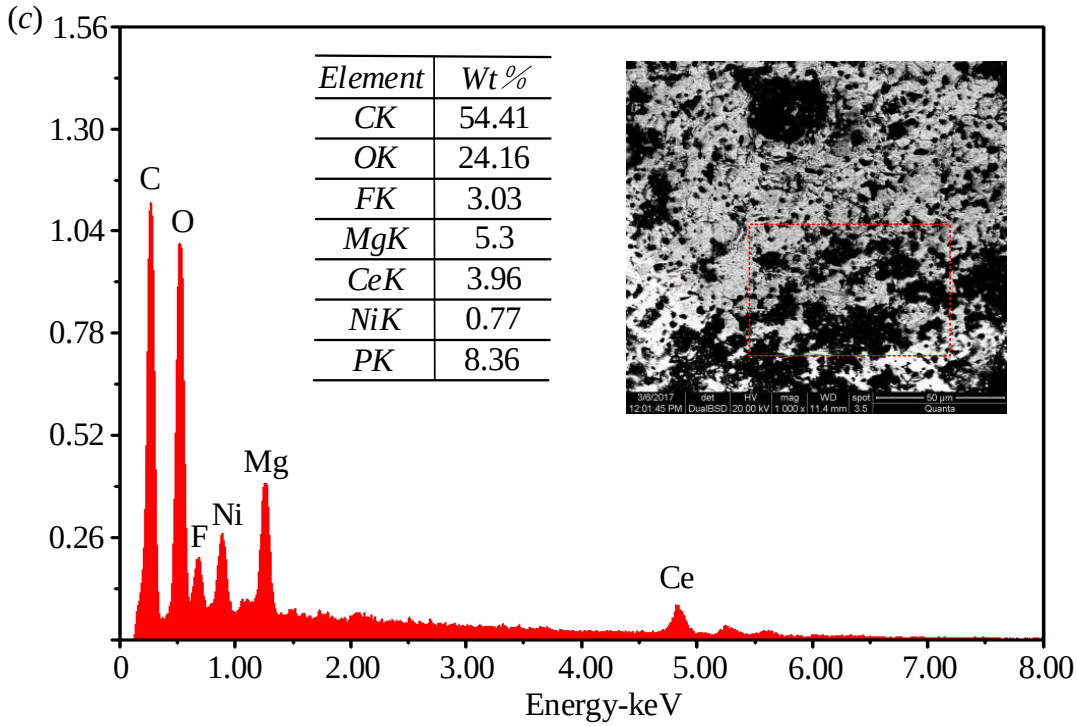

Fig. 8 EDS measurement of chemical element distribution on MgO/CeO_2 surfaces: (a) before grinding, ground surface by grinding wheel (b) I, and (c) II

The change in the surface element distribution of the workpiece before and after grinding is shown in Fig. 9. No new element was found on the surface of the workpiece after grinding with wheel I, but the mass fraction of each original element changed. The mass fraction of C element changed from 6 % to 10.16 %; O element changed from 19.98 % to 19.21 %; the Mg element changed from 17.92 % to 8.61 % and Ce element changed from 55.42 % to 61.9 %.

The mass fraction of C on the surface of the workpiece ground by wheel II changed from 6 % to 54.41 %; O changed from 19.98 % to 24.16 %; Mg changed from 17.92 % to 3.96 % and Ce changed from 55.42 % to 8.36 %. The newly existing Ni and P whose mass fraction were 5.3 % and 0.77 %, respectively, were detected. The mass fraction of each element changed significantly and the change in C and Ce was the most remarkable.

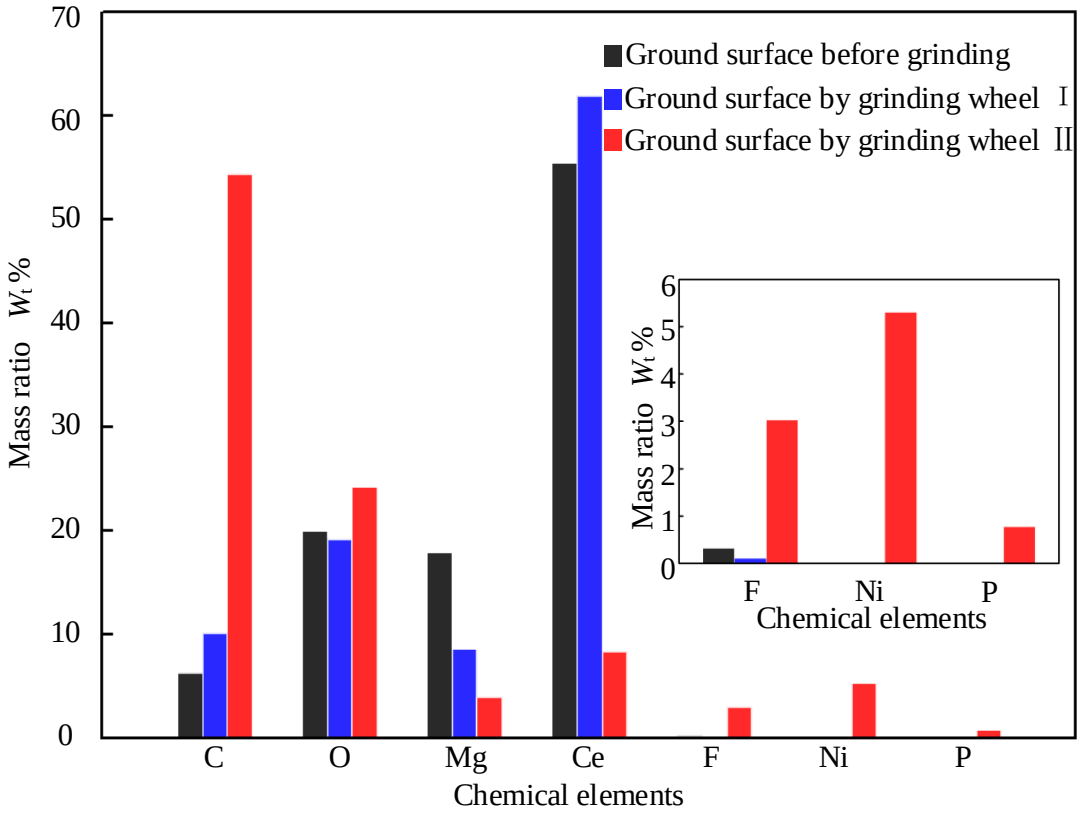

Fig. 9 Contrast of chemical element distribution

5. Discussion

The temperature rise on the workpiece surface during grinding is the result of numerous heating actions of individual abrasive grains on the rotating wheel surface. The transient temperature at the top of the wear flat area of a single grain would be considerably higher than that on the overall workpiece surface, thereby causing a chemical reaction at the local contact area. Fig. 10 compares the temperature rise on the workpiece surface and the transient temperature jump at the top of the wear flat area of an average abrasive grain via calculations by using the established thermal model. The temperature calculated from the temperature field model and measured by thermocouple indicated the increase in grinding temperature. In the present study, it can be controlled within 100 ºC by reasonably selecting the processing parameters (v_s = 15.7 m/s, v_w = 30 mm/s, a_p = 30 μm), thereby ensuring that the workpiece did not exhibit

a have grinding burn. However, the transient temperature at the top of the wear flat area was approximately 1500 °C according to Formula 12 (Fig. 10).

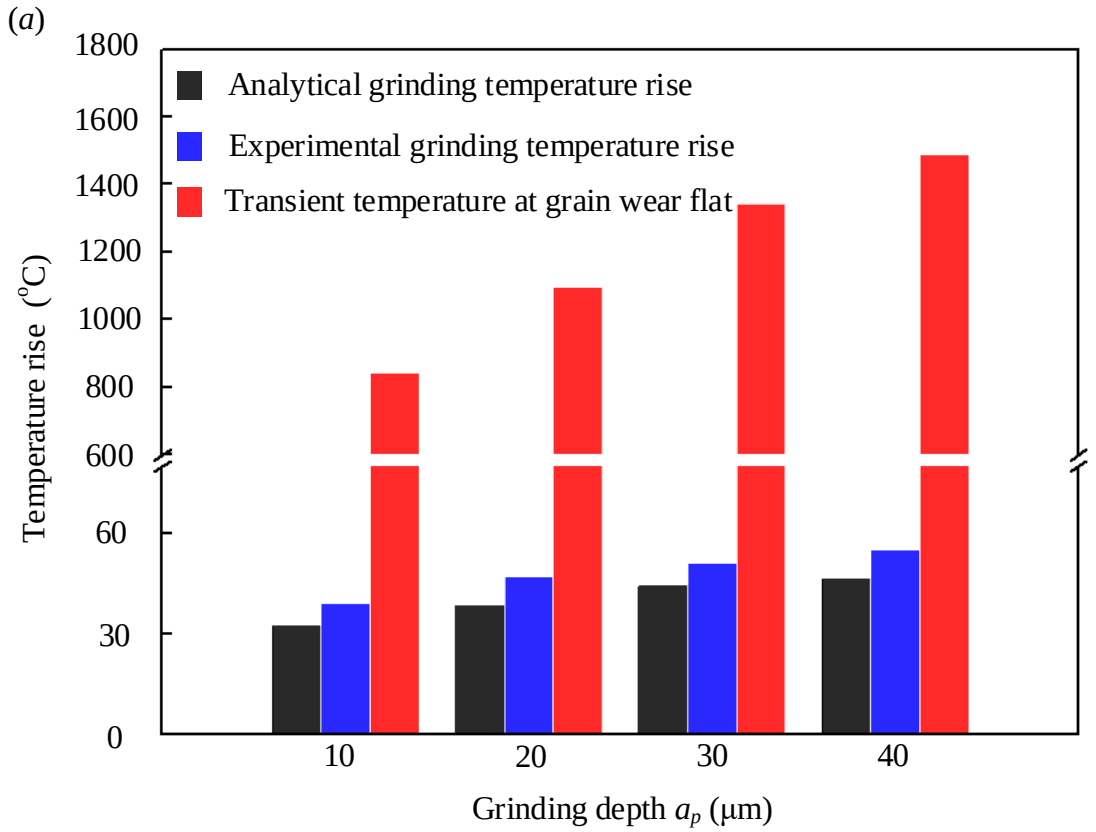

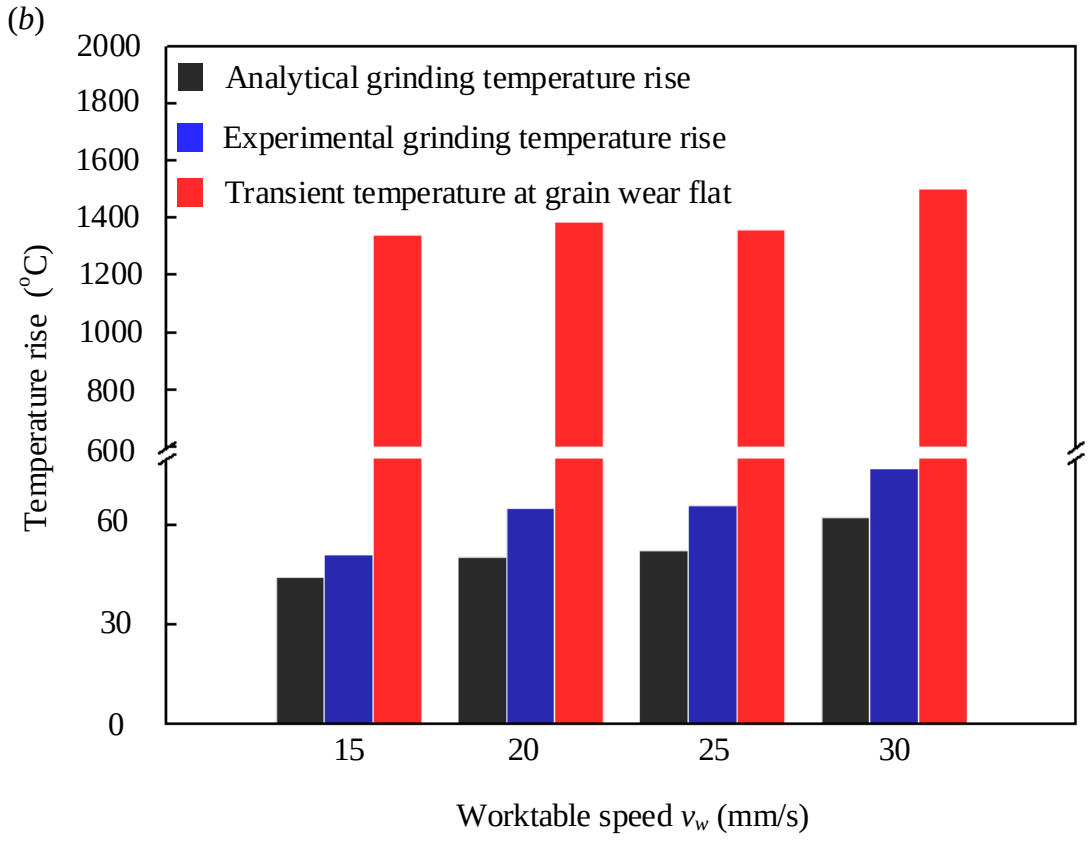

Fig. 10 Comparison of temperature rise on the workpiece surface and transient temperature jump at grain wear flat (a) with grinding depth under v_s = 15.7 m/s, v_w = 15 mm/s and (b) with machining tool worktable speed under v_s = 15.7 m/s, a_p = 30 μm

The high–temperature graphitised the diamond abrasive surface of grinding wheel I [23]. Part of the generated graphite remained on the surface of the workpiece, and another part reacted with MgO at temperatures higher than 1000 ºC. Thus, Mg and CO were generated [24]. CeO_2 underwent a redox reaction with CO and generated Ce_2O_3 and CO_2, as shown in the following equations [25]:

$$MgO + C \rightarrow Mg\uparrow + CO\uparrow \quad (1)$$

$$CeO_2 + CO \rightarrow Ce_2O_3 + CO_2\uparrow \quad (2)$$

Given that the above reaction occurred only negligibly in the contact points, the mass fraction of C and Ce on the surface of the workpiece after grinding by wheel I

was slightly increased, and Mg was slightly decreased (Figs. 8b and 9).

The surface of the diamond abrasive particles in the grinding wheel II was covered with a layer of Ni–P alloy. During grinding, the Ni–P alloy layer was quickly removed by the workpiece because of its low strength after contact with the workpiece. Thus, the diamond surface was directly in contact with the workpiece. The chemical reaction was the same as the former process, but it was intensified because of Ni and P catalysis. Therefore, the mass fraction of each element on the surface of the workpiece changed after grinding by wheel II (Figs. 8c and 9) compared with grinding with wheel I.

As shown in Fig. 11, in the Ni–P alloy layer wrapped around the abrasive particles and in contact with the workpiece, a gap with diamond abrasive appeared and peeled off from the diamond abrasive particles under the repeated action of mechanical force. Part of the fragment of the Ni–P alloy layer was carried away from the grinding zone with the grinding debris, and another part remained on the machined surface, resulting in the uneven distribution of light and heavy elements on the machined surface (Fig. 7c). Ni–P–C chemical bonds were formed between the alloy and the diamond abrasive particles because of the strong infiltration of Ni–P alloy and diamond. The stripped pieces contain Ni, P and abundant C. Hence, Ni and P found on the surface of the workpiece after grinding with wheel II and resulted in the remarkable changes in the mass fraction of C and Ce (Figs. 8c and 9).

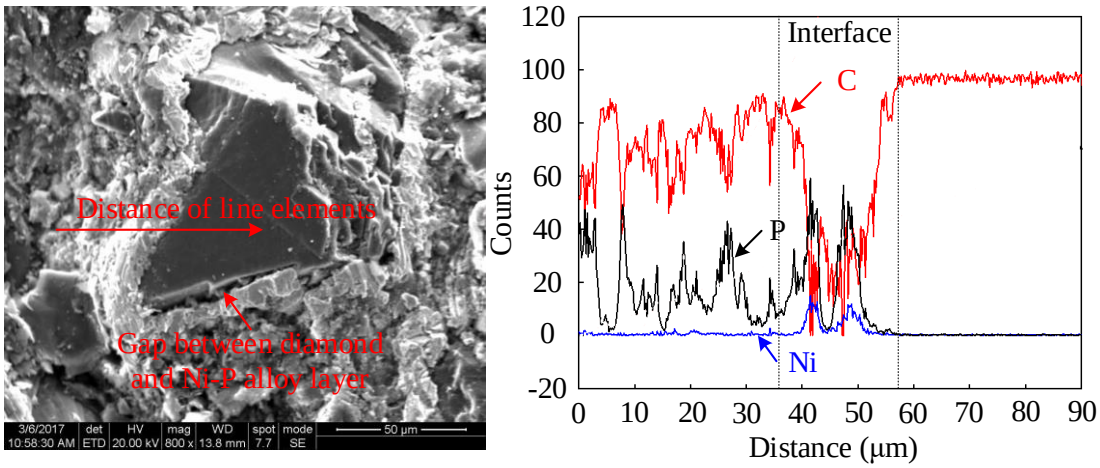

Fig. 11 Typical diamond grit wear of grinding wheel II

5. Conclusions

Thermal damage control issues in the dry grinding of MgO/CeO_2 glass ceramic, including thermal model establishment and potential chemical reaction because of the transient temperature jump at the grain wear flat area were investigated in the present work. The following conclusions were drawn:

1. A temperature model was established and experimentally verified. The model can be used to predict the grinding temperature on the workpiece surface and the transient temperature at the top of the wear flat area in the grinding zone.

2. On the basis of the grinding temperature model, the grinding temperature on the workpiece surface in the grinding zone can be controlled below 100 °C at room temperature to prevent thermal burns by optimising the grinding parameters.

3. Compared with the resin–bond diamond grinding wheel, the wheel with Ni–P alloy coating on the diamond grains intensified the redox reaction because of the catalysis of Ni and P at the transient temperature jump when abrasive particles were cut along the workpiece surface. The mass fraction of each element on the workpiece surface showed an obvious uneven distribution because of the surface spalling of the Ni–P alloy.

4. The optimal process parameters for controlling the grinding zone temperature should be set and a proper grinding wheel should be chosen to avoid the catalytic elements, such as Ni and P, and to avoid thermal damage when grinding the MgO/CeO_2 glass ceramic.

Acknowledgements

This work was supported by the National Science and Technology Major Project of China [No. 2014ZX04001191].

References

[1] María M, Gómez R, Hernández JG, Zúniga A, Germán C, Flores S (2013) Advances in the transesterification of triglycerides to biodiesel using MgO–NaOH, MgO–KOH and MgO/CeO_2 glass ceramics as solid basic catalysts. Catalysis Today 212: 23–30.

[2] Haznan A, Ahn BS, Kim CS, Yoo KS (2007) Preparation and Characterization of MgO–CeO_2 Mixed Oxide Catalysts by Modified Coprecipitation Using Ionic Liquids for Dimethyl Carbonate Synthesis. Industrial & Engineering Chemistry Research 46: 7936–7941.

[3] Sato S, Takahashi R, Sodesawa T, Matsumoto K, Kamimura Y (1999) Ortho–Selective Alkylation of Phenol with 1 – Propanol Catalyzed by CeO_2–MgO. Journal of Catalysis 184: 180–188.

[4] Yang HT, Yang GT, Yuan RZ (1996) The role of MgO–CeO_2 in the densification of Si_3N_4. Journal of Wuhan University of Technology Materials Science 3: 1–7.

[5] Li X, Li B, Li XY, Dai B, Feng YB, Yang J, Qiu T (2016) Effect of MgO/CeO_2 glass ceramics Additives on the Densification and Thermal Conductivity of SiC Multiphase Ceramics with High SiC Content. Journal of synthetic crystals 45: 361–365.

[6] Huang H, Chen WK, Yin L, Xiong Z, Liu YC, Teo PL (2004) Micro/meso ultra precision grinding of fibre optic connectors. Precision Engineering 28: 95–105.

[7] Yi J, Jin T, Deng ZH (2019) The temperature field study on the three–dimensional surface moving heat source model in involute gear form grinding. The International Journal of Advanced Manufacturing Technology 103: 3097–3108.

[8] Pang JZ, Li BZ, Liu Y, Wu CJ (2017) Rayleigh heat flux distribution model investigation and workpiece temperature prediction in the cylindrical grinding. The International Journal of Advanced Manufacturing Technology 89: 3231–3241.

[9] Jin T, Rowe WB, David McCormack (2002) Temperatures in deep grinding of finite

workpieces. International Journal of Machine Tools & Manufacture 42: 53–59.

[10] Wang RQ, Dai SJ, Zhang HB, Dong YF (2017) The temperature field study on the annular heat source model in large surface grinding by cup wheel. The International Journal of Advanced Manufacturing Technology 93: 3261–3273.

[11] Zhang X, Lin B, Xi H (2013) Validation of an analytical model for grinding temperatures in surface grinding by cup wheel with numerical and experimental results. International Journal of Heat and Mass Transfer 58: 29–42.

[12] Fang C, Xu X (2014) Analysis of temperature distributions in surface grinding with intermittent wheels. The International Journal of Advanced Manufacturing Technology 71: 23–31.

[13] Lyu Y, Yu H, Wang J, Chen C, Xiang L (2017) Study on the grinding temperature of the grinding wheel with an abrasive phyllotactic pattern. The International Journal of Advanced Manufacturing Technology 91: 895–906.

[14] Xu XP, Malkin S (2001) Comparison of methods to measure grinding temperatures. Journal of Manufacturing Science and Engineering 123: 191–195.

[15] Xie GZ, Huang H (2008) An experimental investigation of temperature in high speed deep grinding of partially stabilized zirconia. International Journal of Machine Tools & Manufacture 48: 1562–1568.

[16] Chen T, Ye ML, Liu SL, Tian SL (2017) Measurement of ultrasonic assisted grinding temperature based on fiber Bragg grating (FBG) sensor. The International Journal of Advanced Manufacturing Technology 93: 2561–2570.

[17] Rowe WB, Black SCE, Mills B, Morgan MN, Qi HS (1997) Grinding temperatures and energy partitioning. Proc Royal Soc Lond A. Proceedings Mathematical Physical & Engineering Sciences 453: 1083–1104.

[18] Cui L, Hao X, Hu X, Lu A (2015) Effects of Y_2O_3 addition on structure and

properties of LZAS vitrified bond for CBN grinding tools application. Ceramics International 41: 9916–9922.

[19] Ren JX, Hua DA (1988) The Principle of Grinding, first ed. Northwestern Polytechnic University Press, Xi'an, pp 66.

[20] Jin T, Stephenson DJ, Rowe WB (2003) Estimation of the convection heat transfer coefficient of coolant within the grinding zone. Proc. Institution of Mechanical Engineers, Part B: Journal of Engineering Manufacture 217: 397–407.

[21] Rowe WB, Black SCE, Mills B (1996) Temperature control in CBN grinding. The International Journal of Advanced Manufacturing Technology 12: 387–392.

[22] Rowe WB (2001) Thermal analysis of high efficiency deep grinding. International Journal of Machine Tools & Manufacture 41: 1–19.

[23] Kennedy CS, Kennedy GC (1976) The equilibrium boundary between graphite and diamond. Journal of geophysical research 81: 2467–2469.

[24] Li K, Tian Y, Chen X, Yang B, Liu D, Xu B, Qu T, Dai Y (2016) Analysis and simulation of MgO behavior in vacuum carbothermic reduction. Chinese journal of vacuum science and technology 36: 742–747.

[25] Hua W, Li J, Ji J, Xing M (2019) In situ studies on ceria promoted cobalt oxide for CO oxidation. Chinese journal of catalysis 40: 656–663.